

Prediction of improved magnetization and stability in Fe_{16}N_2 through alloying

Cite as: J. Appl. Phys. **126**, 093903 (2019); <https://doi.org/10.1063/1.5109571>

Submitted: 10 May 2019 . Accepted: 12 August 2019 . Published Online: 06 September 2019

N. J. Szymanski , V. Adhikari, M. A. Willard, P. Sarin, D. Gall , and S. V. Khare



View Online



Export Citation



CrossMark

Lock-in Amplifiers up to 600 MHz

starting at

\$6,210



 Zurich
Instruments

Watch the Video 

AIP
Publishing

Prediction of improved magnetization and stability in Fe_{16}N_2 through alloying

Cite as: J. Appl. Phys. 126, 093903 (2019); doi: 10.1063/1.5109571

Submitted: 10 May 2019 · Accepted: 12 August 2019 ·

Published Online: 6 September 2019



View Online



Export Citation



CrossMark

N. J. Szymanski,¹  V. Adhikari,¹ M. A. Willard,² P. Sarin,³ D. Gall,⁴  and S. V. Khare^{1,a)}

AFFILIATIONS

¹Department of Physics and Astronomy, University of Toledo, Toledo, Ohio 43606, USA

²Department of Materials Science and Engineering, Case Western Reserve University, Cleveland, Ohio 44106, USA

³School of Materials Science and Engineering, Oklahoma State University, Tulsa, Oklahoma 74106, USA

⁴Department of Materials Science and Engineering, Rensselaer Polytechnic Institute, Troy, New York 12180, USA

^{a)}Author to whom correspondence should be addressed: sanjay.khare@utoledo.edu

ABSTRACT

We study the structural, energetic, electronic, and magnetic properties of $\text{Fe}_{16-x}\text{M}_x\text{N}_2$ alloys, where M represents 3d transition metals Ti, V, Cr, Mn, Co, and Ni, using special quasirandom structures and density functional theory calculations. We describe stabilization of Fe_{16}N_2 resulting from the enhanced occupation of bonding states relative to the corresponding antibonding states as observed from crystal orbital Hamiltonian population analysis. The hybrid HSE06 functional is employed to calculate a magnetic moment of $2.844 \mu_B/\text{Fe}$, agreeing with recent experimental work and suggesting the importance of electronic exchange effects. Upon alloying, magnetization is found to decrease with all transition metals excluding Mn, for which exceptionally strong ferromagnetic coupling is achieved via nitrogen-mediated exchange interactions. We identify a 1.41% magnetization increase at low Mn concentrations coupled with a decrease in formation energy, making $\text{Fe}_{16-x}\text{Mn}_x\text{N}_2$ a suitable candidate for permanent magnet applications. Novel end-member systems of the form M_{16}N_2 are also investigated, with results implying stability and potential synthesizability of all compounds except Ti_{16}N_2 owing to weak metallic bonding among Ti atoms.

Published under license by AIP Publishing. <https://doi.org/10.1063/1.5109571>

I. INTRODUCTION

Coercive materials exhibiting high magnetization are of great importance due to their application in energy-conversion devices, which are used in numerous technologies such as electric motors, generators, and medical equipment.^{1,2} Currently, the vast majority of permanent magnets contain rare-earth elements such as neodymium and samarium. This poses a significant problem, given the limited availability and poor geographical diversity of these materials.^{1,2} Thus, discovering and producing permanent magnets consisting of more abundant elements would prove extremely beneficial. One of the most promising candidates for a rare-earth free magnet is the $\alpha''\text{-Fe}_{16}\text{N}_2$ phase of iron nitride.³

The $\alpha''\text{-Fe}_{16}\text{N}_2$ ordered martensite phase was first synthesized in 1951 by Jack.⁴ Years later, in 1972, this compound attracted a great deal of interest due to a study by Kim and Takashi, which reported a high magnetic moment of $3.0 \mu_B/\text{Fe}$.⁵ In 1991, Sugita *et al.* detected an even larger magnetic moment of $3.5 \mu_B/\text{Fe}$.⁶ More recent experimental studies revealed results which disagreed with

the previous findings, observing magnetic moments on a much lower range of $2.3\text{--}2.6 \mu_B/\text{Fe}$.⁷⁻⁹ In contrast, a 2013 study by Ji *et al.* has produced results showing agreement with the original findings of Kim and Takashi, reporting a magnetic moment of about $3.1 \mu_B/\text{Fe}$.¹⁰ Thus, the true nature and magnitude of magnetization in Fe_{16}N_2 remains a topic of debate.

To provide insight into this issue, a substantial body of theoretical studies focusing on Fe_{16}N_2 has been conducted. Many early works implemented methods based on generalized gradient approximation (GGA) and local density approximation (LDA) to calculate magnetic moments within the material, reporting relatively low values of $2.3\text{--}2.6 \mu_B/\text{Fe}$.¹¹⁻¹⁵ Ji *et al.* demonstrated the potential importance of strong electron localization in Fe_{16}N_2 , the effects of which are underestimated by standard density functional theory (DFT) techniques.¹⁶ Therefore, by introducing additional correlation in the form of a Hubbard U-value, magnetic moments exceeding $3.0 \mu_B/\text{Fe}$ may be achieved. However, Sims *et al.* called into question the high magnetization induced by such large U-values

which are typically chosen in a semiempirical manner.¹⁷ Instead, hybrid functionals and the GW method were employed to study the electronic structure of Fe_{16}N_2 , showing average magnetic moments of 2.86 and $2.66 \mu_B/\text{Fe}$, respectively.¹⁷ The discrepancy between these methods may arise from the choice of screening and mixing parameters implemented within the hybrid functional scheme, and further investigation is required to confirm the accuracy of the corresponding results.¹⁷ As for the underlying mechanism of strong ferromagnetism in this system, numerous theories have been proposed. Sakuma predicted two major causes of the enhanced magnetization in Fe_{16}N_2 relative to bcc Fe.¹² Firstly, the introduction of N atoms leads to volumetric expansion, thus allowing Fe atoms to display magnetic moments closer to that of their known atomic values. Secondly, N sites mediate long-range exchange interactions through “charge hopping” while also decreasing occupation of Fe minority-spin states.¹² Ji *et al.* further built upon this theory by clarifying the roles of both itinerant and localized electrons, made possible by large variations in charge distribution near Fe–N clusters, in the stabilization of global ferromagnetic coupling with high Fe magnetic moments.¹⁶ Sims *et al.* provided electronic structure calculations supporting the importance of N in stabilizing large Fe magnetic moments through increased exchange splitting.¹⁷ In contrast, Ke *et al.* suggested that the theoretical magnetization of Fe_{16}N_2 may not exceed $\sim 2.5 \mu_B/\text{Fe}$, as no significant charge transfer between inequivalent Fe sites is observed within the framework of the quasiparticle self-consistent GW approximation.¹⁸ Therefore, a theoretical consensus has not yet been reached regarding both the magnitude and mechanism of magnetization in Fe_{16}N_2 .^{12,16–18}

Should the large saturation magnetization be verified, Fe_{16}N_2 would be promising for many applications. However, a major issue in this material is its relatively low thermal stability. It has been shown that the α'' -phase of Fe_{16}N_2 decays at temperatures above 525 K,¹⁹ therefore limiting its application as a permanent magnet to low temperatures.²⁰ Despite this shortcoming, there does exist a potential solution. Several experimental and theoretical works have recently reported that alloying Fe_{16}N_2 with certain transition metals can significantly increase its stability. Experimentally, both Mn and Ti have been considered. Wang and Jiang found that Fe_{16}N_2 remained stable up to 1073 K when alloyed with Ti at concentrations of 5%–12%.²¹ Jiang *et al.*²² observed an increase in stability, although to a lesser degree, when Fe_{16}N_2 was alloyed with Mn at concentrations of 5%–15%. Effects of other transition metals have been studied through implementation of theoretical methods. Standard techniques based on GGA and LDA have predicted Ti, Cr, Mn, Co, and Ni to lower the system’s overall formation energy when alloyed at concentrations ranging from 5% to 20%.^{22–25} However, inclusion of these impurities at high concentrations is predicted to decrease the saturation magnetization, which is detrimental for most applications.^{21–25}

Despite a considerable degree of investigation into the properties of $\text{Fe}_{16-x}\text{M}_x\text{N}_2$ alloys, some important gaps of understanding still exist. Firstly, most theoretical studies have utilized GGA and/or LDA,^{22–24} which may underestimate the electron localization and exchange-correlation effects occurring in Fe_{16}N_2 .^{12,16} Secondly, only relatively high alloy concentrations ($\geq 5\%$) have been tested, thus excluding the possibility of nonlinear behavior at lower values.^{21–25} Lastly, several 3d transition metals having the potential

to improve the energetic and/or magnetic properties of Fe_{16}N_2 remain unexplored.

In this work, we study novel $\text{Fe}_{16-x}\text{M}_x\text{N}_2$ alloys with the potential to exhibit improved thermodynamic stability and/or enhanced magnetization. Six 3d transition metals (M) are considered: Ti, V, Cr, Mn, Co, and Ni. These elements are chosen based on previous interest, suitability as substitutional defects, and potential to positively influence the overall properties of Fe_{16}N_2 .^{21–25} To improve upon previous works, we implement several advanced computational techniques. Special quasirandom structures are utilized to more accurately replicate experimental configurations at high temperatures, while hybrid functionals are used to account for charge localization effects in electronic structure and magnetic moment calculations. We focus on the property of magnetization, which is a crucial (though not the only) factor in identifying materials with high coercivity. A wide range of concentrations (6.25%–18.75%) are tested for all alloys, with lower concentrations (as low as 1.5%) investigated for cases of special interest. We aim to explore the possibility of engineering minor magnetization enhancements in Fe_{16}N_2 while maintaining or improving thermal stability.^{16,17,26} Electronic structure and Crystal Orbitals Hamiltonian Populations are also analyzed to provide insight into the underlying mechanism of magnetic coupling and energetic stabilization in $\text{Fe}_{16-x}\text{M}_x\text{N}_2$ alloys.

II. COMPUTATIONAL METHODS

All density functional theory (DFT) calculations have been performed using the Vienna *Ab initio* Simulation Package (VASP).^{27–31} We have utilized the Perdew–Burke–Ernzerhof (PBE) exchange correlation functional based on the generalized gradient approximation (GGA) within the framework of the projector augmented wave (PAW) method.³² A cutoff energy of 520 eV was used for the plane-wave basis set. The Mn_pv and Cr_pv potentials, in which semicore 3p electrons are treated as valence states, were chosen for manganese and chromium, while the Ti_sv and V_sv potentials, in which semicore 3s and 3p electrons are treated as valence states, were chosen for titanium and vanadium. Default potentials, which treat only the outer-core 4s and 3d electrons as valence states, were used for iron, nickel, and cobalt. An $8 \times 8 \times 8$ Monkhorst–Pack k-point grid was employed for calculations involving 18-atom conventional unit cells, whereas even divisions of the grid were constructed throughout the corresponding supercell calculations, e.g., a $4 \times 4 \times 4$ grid for $2 \times 2 \times 2$ supercells. A convergence criterion of 10^{-6} eV with a Gaussian smearing value of width 0.05 eV was chosen for the electronic minimizations. Spin polarization was considered to account for magnetic ordering. Potentially suitable ferromagnetic, antiferromagnetic, and nonmagnetic configurations were tested, while only the lowest energy states were considered for the remaining calculations.

The experimental structure of Fe_{16}N_2 , as determined by Jack,⁴ was geometrically optimized by allowing the unit cell shape, volume, and ionic positions to relax until the force acting on each atom was less than or equal to $0.01 \text{ eV}/\text{\AA}$. To determine ground-state structures of the end-member compounds, the relaxed unit cell of Fe_{16}N_2 , with each transition metal in place of Fe, was fully optimized. To provide insight into dynamic stability, phonon density of states were computed for the end-members. As discussed

throughout many texts,^{33–36} the frequency of a phonon mode represents the second derivative of energy with respect to atomic displacements. Accordingly, real and imaginary (shown as positive and negative here) frequencies correspond to concave and convex energy wells, respectively; systems displaying only real phonon frequencies are, therefore, stable against moderate thermal vibrations allowing experimental synthesis to remain possible. To study these properties, Hessian matrices were calculated on 72-atom supercells using density functional perturbation theory (DFPT).^{27–31} From these values, the PHONOPY software³⁶ was utilized to compute the phonon density of states.

To simulate alloying of $\text{Fe}_{16-x}\text{M}_x\text{N}_2$ at various concentrations, we implemented special quasirandom structures (SQSs), which are capable of sufficiently replicating the properties of random alloys.³⁷ These were generated using the mcsqs code within the Alloy Theoretic Automated Toolkit (ATAT),^{38–43} in which Monte Carlo simulations are performed to sample many unique configurations with the goal of minimizing the differences between correlations of the SQSs and those of perfectly random alloys. This is done using cluster expansion formalism, for which correlations are broken down into individual pairs, triplets, quadruplets, and so forth. A more detailed explanation of the methods used may be found in the works of Zunger *et al.*³⁷ and van de Walle *et al.*^{38–41} Here, we use the 9-atom primitive cell of Fe_{16}N_2 as a preliminary structure. To match desired correlations at each concentration, supercells were created with sizes of 36, 72, or 144 atoms, depending on the concentration. We created SQS with atomic concentrations, defined as the number of alloy atoms (M) divided by the total number of metal atoms ($\text{Fe} + M$), ranging from 0.0% to 18.75% in intervals of 3.125%. All structures were fully geometrically optimized.

High-precision static calculations were performed on end-member and alloyed compounds to obtain accurate final energies. These were then used to calculate the formation energy of each material, defined as the difference between the energy of the compound and the energies of its constituents in their respective ground states. Accordingly, the following equation was used:

$$\Delta E_{\text{form}}(x) = (1/18)E(\text{Fe}_{16-x}\text{M}_x\text{N}_2) - (16-x)E(\text{Fe}) - E(\text{N}_2) - xE(\text{M}), \quad (1)$$

where x corresponds to the alloy concentration ($0 \leq x/16 \leq 0.1875$) and $E(M)$ represents the energy of the ground state of each transition metal; these include the hexagonal-close-packed structure for Ti and Co, the body-centered-cubic structure for V, Cr, Mn, and Fe, and the face-centered-cubic structure for Ni. For the energy of nitrogen $E(\text{N}_2)$, a single dimer (N_2) simulated within a large cell was considered. In all cases, lattice parameters and internal atomic positions are fully relaxed using the aforementioned methods to obtain consistency in comparison of energies.

Generally, standard exchange-correlation functionals based on GGA and LDA perform well when used to compute structural, electronic, and magnetic properties of purely metallic systems.^{44,45} For instance, GGA has been shown to predict a magnetic moment of $2.23 \mu_B/\text{Fe}$ in bcc Fe, which is in close agreement with the experimental value of about $2.2 \mu_B/\text{Fe}$.¹⁷ In contrast, when dealing with materials exhibiting any significant degree of valence electron

localization, both GGA and LDA tend to display some faults. Though their prediction of equilibrium structure remains relatively accurate, these methods consistently underestimate properties such as bandgaps and magnetic moments.^{44,45} Such errors may be reduced by employing methods such as DFT + U, hybrid functionals, and GW, which typically work well when applied to semiconductors and insulators.⁴⁵ However, their accuracy in metals varies depending on subtle properties based on exchange-correlation effects and the degree of electron localization.⁴⁶ For example, both the Heyd-Scuseria-Ernzerhof hybrid (HSE06) functional⁴⁷ and the self-consistent GW method overestimate the magnetic moment of bcc Fe by about 0.66 and $0.50 \mu_B/\text{Fe}$, respectively, owing to the highly delocalized nature of the electrons.¹⁷ In contrast to these completely itinerant ferromagnetic materials, electron localization is generally agreed to play a greater role in Fe_{16}N_2 .^{12,16} Therefore, hybrid functionals and the GW method are likely more suitable to describe this system, though results should be taken cautiously as discussed in detail by Sims *et al.*¹⁷ In this work, we choose to employ the hybrid HSE06 functional in calculating electronic and magnetic properties. Within the HSE06 formalism, the exchange-correlation energy is given by⁴⁷

$$E_{xc} = \frac{1}{4}E_x^{\text{HF,SR}}(\omega) + \frac{3}{4}E_x^{\text{PBE,SR}}(\omega) + E_x^{\text{PBE,LR}}(\omega) + E_C^{\text{PBE}}. \quad (2)$$

Accordingly, the correlation term is treated entirely by PBE whereas 25% of the short-range exchange is calculated using the exact Hartree-Fock exchange. In HSE06, the screening parameter ω is chosen to be 0.2 \AA^{-1} allowing for treatment of metallic systems.⁴⁷ We note that although hybrid functionals generally provide improved agreement with experimental data in most cases, the physical origin of the results may differ considering that electron correlation is only treated within GGA.^{45–47} Hence, implications of fundamental properties based on the electronic structure calculated using hybrid functionals must be considered carefully.

III. RESULTS AND DISCUSSION

A. Structural details

The crystal structure of α' - Fe_{16}N_2 is body-centered-tetragonal with space group $I4/mmm$.⁴ The unit cell can be constructed by considering a $2 \times 2 \times 2$ supercell of body-centered-cubic Fe, with N atoms inserted interstitially into the lattice. The addition of the N atoms leads to an expansion of the unit cell, more so in one axial direction, leading to the body-centered-tetragonal form with slight distortions to the Fe site positions away from body-centered-cubic positions. Within the Fe_{16}N_2 unit cell, the 16 Fe atoms can be divided into three symmetrically inequivalent groups: four $4e$ sites, eight $8h$ sites, and four $4d$ sites. The crystal structure of Fe_{16}N_2 is displayed in Fig. 1.

Our calculated lattice parameters for the unit cell of pure Fe_{16}N_2 are $a = 5.672 \text{ \AA}$ and $c = 6.231 \text{ \AA}$, corresponding to $c/a = 1.098$ and a volume of 200.486 \AA^3 . Hence, the introduction of interstitial N atoms leads to an expansion of about 7% with respect to bcc Fe. Our results match well with the corresponding experimental values of $a = 5.72 \text{ \AA}$, $c = 6.29 \text{ \AA}$, $c/a = 1.0997$, and $V = 206 \text{ \AA}^3$.⁴⁸ Previous

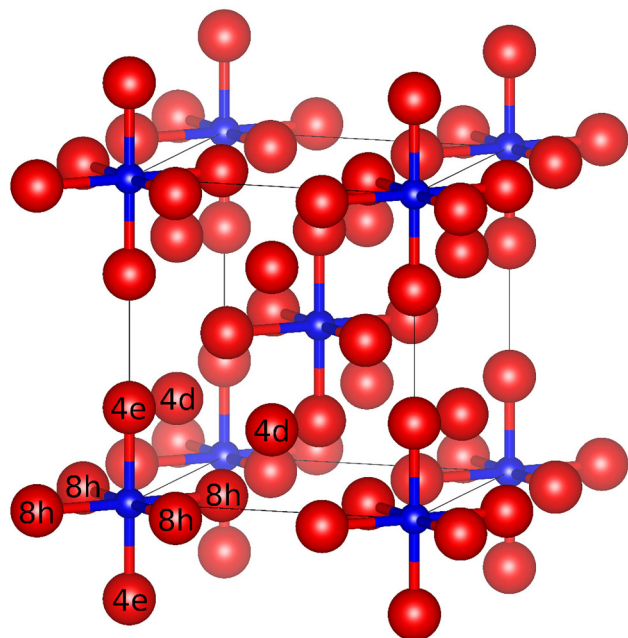


FIG. 1. The unit cell of α' -Fe₁₆N₂.⁷⁶ The large red spheres represent Fe atoms, while the small blue spheres represent N atoms. The three symmetrically inequivalent Wyckoff sites are labeled: 4e, 8h, and 4d.

computational works have also reported satisfactory agreement with experiment.^{23,24,49}

Calculated lattice parameters as a function of alloy concentration for each Fe_{16-x}M_xN₂ system are shown in Fig. S1 of the [supplementary material](#). There appear to be some consistent trends as alloy concentration is increased. The most noticeable effect is an increase in the c/a ratio, occurring for all elements except V and Co, for which the former exhibits a minor decrease in c/a at high V concentrations. Generally, substitution of impurity transition metal atoms into the lattice causes an expansion of the c -axis while the a -axis either increases or decreases to a much lesser degree. We note that contraction or expansion along the a -axis can be directly related to the atomic radius of each transition metal, whereas changes in the c -axis are found to be more independent of ionic size; instead they show greater correlation with the nature of magnetic coupling as will be described in Sec. III C, therefore providing an explanation of the unique properties arising from alloys with Co and V. Regarding the change in volume of Fe_{16-x}M_xN₂ alloys, effects are strongly dependent on the choice of transition metal. For Ti and V, increasing concentration leads to relatively large expansion. Mn also causes a volume increase; however, the magnitude is much smaller. The remaining three elements (Co, Cr, and Ni) cause only a slight decrease in the cell size. These effects can be directly linked to the atomic radius of each element. Our results are consistent with those of previous works. Huang *et al.*²³ and Benea *et al.*²⁵ have also demonstrated a direct relationship between the volume of Fe_{16-x}M_xN₂ alloys and the corresponding atomic radii of the

elements $M = \text{Ti, Cr, Mn, Co, and Ni}$, while the a - and c -axes were found to vary anisotropically. Furthermore, Zhao *et al.*²⁴ suggested that changes in c/a may be more closely related to underlying magnetic interactions, in agreement with our findings. Regarding the magnitude of change in lattice parameters for each alloy, minor differences between the data calculated in this work and values found previously²³⁻²⁵ display minor differences owing to disordering effects created by utilization of SQS.

Optimized lattice parameters have also been computed for the end-member compounds. Except for Fe₁₆N₂, none have been synthesized experimentally, and we, therefore, present purely predictive findings. Structural data can be found in Table S1 of the [supplementary material](#). All compounds, except for Co₁₆N₂, maintain the tetragonal Fe₁₆N₂-type structure with space group $I4/mmm$. Ti₁₆N₂, Cr₁₆N₂, and V₁₆N₂ display large c/a ratios similar to that of Fe₁₆N₂ (~ 1.1). In contrast, Mn₁₆N₂ and Ni₁₆N₂ exhibit exceptionally large c/a ratios of about 1.4. As will be discussed in Sec. III B, these are also the only compounds to display any significant degree of magnetization (excluding Co₁₆N₂ and Fe₁₆N₂), thus supporting the hypothesis that magnetic effects play the largest role in the tetragonality of these systems. In Co₁₆N₂, we predict a tetragonal-to-cubic transition, in agreement with previous findings.²⁴ This phenomenon can also be attributed to magnetic effects, as the strong magnetization in Fe_{16-x}Co_xN₂ coupled with an increase in c/a ratio results in structural instability at concentrations near 50%.²³ Regarding the cell size of end-member compounds, volume decreases monotonically for elements moving left to right across the $3d$ row, showing direct relation to atomic radii and electronegativities.

To determine whether these materials could potentially be synthesized experimentally, we have computed the phonon density of states for each compound, displayed in Fig. S2 of the [supplementary material](#). Fe₁₆N₂ is characterized by a strong presence of acoustic phonon modes below 8 THz and optical modes with small bandwidths centered around 11, 14, and 22 THz. These features match well with previous findings.²⁴ For all other end-members, acoustic modes exhibit similar frequencies. However, optical mode frequencies, deriving mainly from vibrations of the lighter nitrogen atoms ($m_N \approx 14.007$ u), are strongly dependent on the compound. Materials consisting of lighter transition metals, such as V ($m_V \approx 50.942$ u) and Cr ($m_{Cr} \approx 51.996$ u), display nondegenerate sets of optical modes with frequencies as high as 25 THz. In contrast, those containing heavier metals, such as Co ($m_{Co} \approx 58.933$ u) and Ni ($m_{Ni} \approx 58.693$ u), exhibit degenerate optical modes with lower frequencies in the range of 17–18 THz owing to minimal differences between masses of the metal and nitrogen atoms. With respect to stability, all compounds excluding Ti₁₆N₂ exhibit only real-valued frequencies, indicating dynamical stability, and, therefore, suggesting the possibility of experimental synthesizability. Considering that Ti is furthest left on the periodic table out of all $3d$ transition metals considered, instability in Ti₁₆N₂ can be attributed to its low valence electron concentration. As a result, the strength of the metallic Ti–Ti bonds (discussed in Sec. III D) will be insufficient to maintain the expanded body-centered-tetragonal structure. Instead, we speculate that it will likely adopt a more close-packed configuration, which would be in agreement with the hexagonal structure of Ti in its ground state, contrasting the bcc structures of most other $3d$ transition metals.⁴⁹

B. Formation energy

The formation energy of pure Fe_{16}N_2 is predicted to be -0.2136 eV/atom, which agrees very well with previous findings.⁵⁰ Formation energies of each $\text{Fe}_{16-x}\text{M}_x\text{N}_2$ alloy as a function of concentration are displayed in Fig. 2, with exact values listed in Table S2 of the supplementary material. Our findings indicate that all elements in this work lead to a more negative formation energy, therefore stabilizing the material. Ti and V have the greatest effect; when alloyed at a concentration of 18.75%, Ti and V cause the formation energy to decrease by about 0.15 eV/atom and 0.106 eV/atom, respectively, corresponding to significant changes of -77.0% and -47.3% when compared to the initial energy of Fe_{16}N_2 . The Boltzmann approximation gives $\Delta E_F \sim k_B \Delta T$ where k_B is Boltzmann's constant, ΔE_F is the change in formation energy, and ΔT is the change in decomposition temperature. Assuming these results directly translate to thermodynamic stability; the alloys containing Ti and V at concentrations of 18.75% may remain stable up to temperatures of about 930 K and 775 K under the Boltzmann approximation, therefore making these compositions very suitable choices if one wishes to stabilize Fe_{16}N_2 for high-temperature applications. The remaining elements Mn, Co, Ni, and Cr also cause a decrease in formation energy; however, the magnitude is much less than that of Ti and V. When alloyed at 18.75%, the change in energy ranges from -0.0056 eV/atom to -0.015 eV/atom, corresponding to relatively small decreases of 2.5% and 6.7%, respectively. In general, $\text{Fe}_{16-x}\text{M}_x\text{N}_2$ formation energy as a function of concentration follows a mostly linear relationship, with only minor deviations. Detailed explanations of the energetic effects for each metal are described in Sec. III D. Our results corroborate experimental findings which have shown that $\text{Fe}_{16-x}\text{M}_x\text{N}_2$ alloys are stabilized for $M = \text{Mn}$ and Ti, while also clarifying the magnitude to

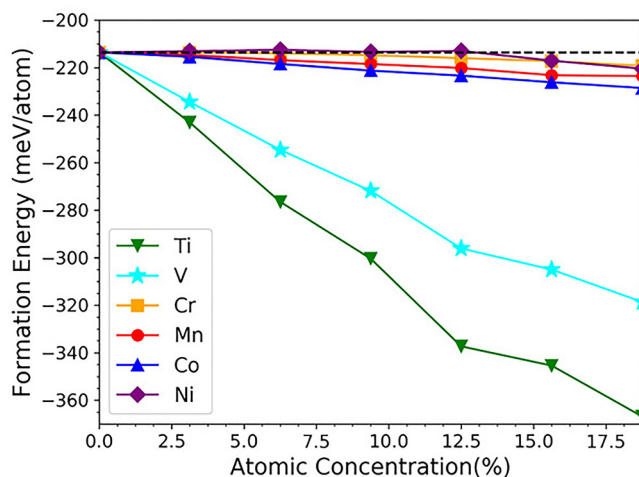


FIG. 2. Formation energies of $\text{Fe}_{16-x}\text{M}_x\text{N}_2$ calculated using GGA. M represents Ti, V, Cr, Mn, Co, and Ni. Alloy concentrations listed are given by $(x/16) \times 100\%$. Values are normalized per total number of atoms in the simulation cell. The dashed black line represents the formation energy of pure Fe_{16}N_2 . Each point represents a calculated value, whereas the lines are interpolations.

which they do so.^{20,21} Several previous theoretical studies have reported formation energies for fully-ordered $\text{Fe}_{16-x}\text{M}_x\text{N}_2$ alloys with $M = \text{Ti}, \text{Cr}, \text{Mn}, \text{Co},$ and Ni , showing general improvements to the stability of Fe_{16}N_2 .²²⁻²⁵ However, Huang *et al.* demonstrated the importance of occupation site ($4e$, $4d$, or $8h$), by which cohesive energy is influenced and may be increased for the cases of Co and Ni placed at $4d$ sites.²³ In this work, we find that random occupation in the SQS allows for a relatively energetically favorable configuration to form, indicating the importance of disorder in the improved stability of Fe_{16}N_2 .

Formation energies of the end-member systems were also computed and are listed in Table S2 of the supplementary material. All compounds are predicted to exhibit formation energies lower than that of Fe_{16}N_2 . The energy of each end-member matches well with trends of the respective $\text{Fe}_{16-x}\text{M}_x\text{N}_2$ alloy, thus providing further evidence that the formation energy follows a mostly linear path as concentration is increased from 0.0% to 100.0%.

C. Magnetic moment

Magnetic moments in all $\text{Fe}_{16-x}\text{M}_x\text{N}_2$ alloys were computed using both GGA and the hybrid HSE06 functional. For pure Fe_{16}N_2 , GGA predicts an average magnetic moment of $2.413 \mu_B/\text{Fe}$, agreeing with previous works which have implemented similar methods, e.g., $2.35 \mu_B/\text{Fe}$ using LDA^{11,13,14} and $2.4-2.45 \mu_B/\text{Fe}$ using GGA.^{12,17,18} In contrast, the HSE06 functional predicts a much larger moment of $2.844 \mu_B/\text{Fe}$ owing to increased charge localization and exchange splitting, to be discussed in greater detail throughout Sec. III D. Our findings match the work of Sims *et al.*, in which the HSE06 functional is used to predict a magnetic moment of $2.86 \mu_B/\text{Fe}$.¹⁷ In contrast, the GW method has been shown to give lower moments in the range $2.59-2.66 \mu_B/\text{Fe}$, suggesting that hybrid functionals may overestimate exchange splitting effects.^{17,18} However, considering the most recent experimental work of Ji *et al.* which has reported high magnetic moments on the order of $3.1 \mu_B/\text{Fe}$,¹⁰ the HSE06 functional appears to provide reasonably reliable results with respect to the magnetization of Fe_{16}N_2 .

Local Fe magnetic moments at the $4d$, $4e$, and $8h$ sites, predicted using the HSE06 functional, are determined to be 2.955, 2.739, and $2.823 \mu_B$, respectively. Variations between inequivalent sites can be attributed to local bonding environments. Each N atom is coordinated by six Fe atoms occupying the $4e$ and $8h$ sites. The d orbitals of these Fe atoms display strong hybridization with the p orbitals of N, leading to a significant degree of electron localization within the Fe-N clusters. In contrast, Fe atoms at the $4d$ sites are surrounded only by Fe atoms at $4e$ and $8h$ sites. This leads to a metallic environment consisting of itinerant spin-up electrons, while some spin-down electrons are transferred to neighboring Fe atoms having some unoccupied orbitals due to their interaction with N. As a result, Fe atoms at the $4d$ site achieve very high magnetic moments. These conclusions agree with the theoretical description of magnetism in Fe_{16}N_2 as proposed by Ji *et al.*,¹⁶ while the magnitude of magnetic moment at each site matches with those calculated using HSE06 by Sims *et al.*¹⁷ Similarly, although GW predicts an overall lower magnetization, the moments at the $4d$, $4e$, and $8h$ sites relative to one another agree with the differences found in this work,¹⁸ thus illustrating the importance of charge

variations throughout the structure of Fe_{16}N_2 . We also compare the magnetic moments found with HSE06 to those obtained using GGA to further elucidate the potential effects of electron localization around each Fe site. At the $4d$ sites, the magnetic moment is increased by a relatively small amount ($\sim 0.26 \mu_B$) when implementing HSE06 as opposed to GGA, whereas the $4e$ and $8h$ sites exhibit very large increases ($\sim 0.65 \mu_B$). This supports current theories suggesting that electron localization plays a much larger role in Fe atoms at the $4e$ and $8h$ sites.¹⁶ Within the framework of the HSE06 functional,⁴⁷ enhanced localization arises from exchange interactions mediated by the interstitial N atoms.¹⁷ However, whether such a description accurately represents the underlying physics occurring in Fe_{16}N_2 remains unclear, and further investigation is necessary to clarify exchange and correlations effects.

Magnetic moments for $\text{Fe}_{16-x}\text{M}_x\text{N}_2$ alloys were computed using both GGA and HSE06, each predicting similar trends. As results obtained within the framework of GGA have previously been reported for most alloys in this work,^{23–25} we instead focus on those calculated using the HSE06 functional. Three concentrations (6.25%, 12.5%, and 18.75%) are tested to conserve computational resources. Average magnetic moments are listed in Table I. Excluding the unique case of Mn from consideration, the transition metals may be divided into two groups: (i) Those which lie to the left of Fe on the periodic table (Ti, V, Cr) and cause a relatively large decrease in magnetic moment. (ii) Those which lie to the right of Fe (Co, Ni) and cause only a small decrease in magnetic moment. $\text{Fe}_{16-x}\text{M}_x\text{N}_2$ alloys with high concentrations (18.75%) of transition metals in group (i) exhibit average magnetic moments which are about 30% lower than that of pure Fe_{16}N_2 . In contrast, alloys with the same concentration of metals in group (ii) display moments which are only 5%–15% lower than Fe_{16}N_2 . We find these effects to be directly related to the nature of magnetic coupling, which can be determined by analyzing the local magnetic moment of impurity atoms with respect to neighboring Fe atoms. Our results indicate that elements in group (i) couple antiferromagnetically, i.e., their magnetic moments align antiparallel to those of surrounding Fe atoms. Ti, V, and Cr achieve average moments of -1.263 , -2.218 , and $-3.152 \mu_B$, respectively. Hence, moving left to right across the row allows more unpaired d electrons to become available, leading to an increase in the magnitude of the antiparallel magnetic moments.

TABLE I. Magnetic moments of $\text{Fe}_{16-x}\text{M}_x\text{N}_2$ alloys calculated using the hybrid HSE06 functional. M represents the $3d$ transition metals Ti, V, Cr, Mn, Co, and Ni. Alloy concentrations listed are given by $(x/16) \times 100\%$. Each moment is the average for all metals within the structure, including both Fe and M. Magnetic moments of end-member compounds, i.e., at M concentrations of 0% and 100%, are also listed.

| Average $\text{Fe}_{16-x}\text{M}_x\text{N}_2$ local magnetic moments (μ_B) | | | | | |
|---|-------|-------|-------|--------|---------|
| Element | 0.00% | 6.25% | 12.5% | 18.75% | 100.00% |
| Mn | 2.844 | 2.843 | 2.842 | 2.840 | 0.188 |
| Co | 2.844 | 2.812 | 2.719 | 2.688 | 1.937 |
| Ti | 2.844 | 2.500 | 2.219 | 1.938 | 0.000 |
| Cr | 2.844 | 2.406 | 2.031 | 1.938 | 0.031 |
| V | 2.844 | 2.469 | 2.125 | 1.812 | 0.094 |
| Ni | 2.844 | 2.657 | 2.625 | 2.469 | 0.718 |

As for elements in group (ii), the impurity atoms are found to couple ferromagnetically, i.e., their magnetic moments align parallel to those of surrounding Fe atoms. Co and Ni achieve average moments of 1.836 and $0.771 \mu_B$, respectively. In contrast to the group (i) elements, moving left to right across the row causes more electrons to become paired, leading to a decreased magnetic moment. Further analysis of these effects is provided in Sec. III D.

By considering changes in volume as a function of concentration, discussed in Sec. III A, we have also computed the volume magnetization of each alloy. Results are displayed in Fig. 3, with exact values listed in Table S3 of the supplementary material. We find that Fe_{16}N_2 exhibits a magnetization of approximately 2.103 MA/m. As for the alloys, incorporating volume effects has only a small impact on the magnetization, i.e., the change in magnetic moment plays a much larger role. The magnitude of the decrease in magnetization for $\text{Fe}_{16-x}\text{M}_x\text{N}_2$ with $M = \text{Cr, Co, and Ni}$ is lessened by contraction of unit cell as concentration is increased. For $M = \text{Ti and V}$, magnetization is decreased to a greater degree as a result of volume expansion. Our findings here build upon recent studies such as those of Huang *et al.*²³ and Benea *et al.*,²⁵ in which GGA has been utilized to predict significant decreases in magnetization for alloys with Ti and Cr, as well as much less substantial magnetization effects for alloys with Mn, Co, and Ni. Furthermore, Ke *et al.* have shown similar behavior using the GW method.¹⁸ Considering our results obtained using the HSE06 functional match with the aforementioned findings, we conclude that although the magnitude of magnetic moment may vary depending on the method used, trends with respect to alloy concentration generally remain consistent.

As shown in Fig. 3, Mn represents an outlier in the data. The magnetic moment of $\text{Fe}_{16-x}\text{Mn}_x\text{N}_2$ remains nearly constant for

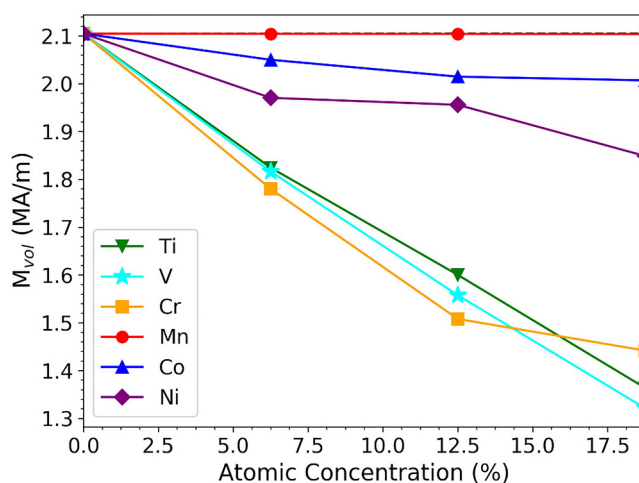


FIG. 3. Calculated volume magnetization (M_{vol}) of $\text{Fe}_{16-x}\text{M}_x\text{N}_2$ calculated using the hybrid HSE06 functional. M represents Ti, V, Cr, Mn, Co, and Ni. Alloy concentrations listed are given by $(x/16) \times 100\%$. The dashed black line represents the magnetization of pure Fe_{16}N_2 . Each point represents a calculated value, whereas the lines are interpolations.

concentrations up to 18.75%. As with the other elements, this effect is directly related to the nature of magnetic coupling. We find that Mn couples ferromagnetically with Fe and achieves a very high average magnetic moment of $3.43 \mu_B$. Although this value is greater than that of the Fe atoms, introduction of Mn also causes a slight decrease in the magnetic moments of surrounding Fe atoms. Therefore, the large moment of Mn and decreased moment of Fe cancel one another out, resulting in an unchanged average magnetic moment. Further explanation of this phenomenon is provided in Sec. III D. To determine whether this trend continues, we have tested higher concentrations of Mn. We find that at concentrations of 25% and higher, the magnetic moment of $\text{Fe}_{16-x}\text{Mn}_x\text{N}_2$ begins to deteriorate substantially. More specifically, the average magnetic moment drops to about $2.56 \mu_B$, $1.83 \mu_B$, and $1.09 \mu_B$ at Mn concentrations of 25%, 50%, and 75%, respectively. This is caused by a change in the nature of magnetic coupling; at concentrations of 25% and above, a small percentage of Mn atoms begin to couple antiferromagnetically, displaying large antiparallel magnetic moments ranging from about -3.1 to $-3.8 \mu_B$. Additionally, as concentration is increased, the percentage of Mn atoms coupling antiferromagnetically increases as well. These findings are reminiscent of many previous studies; the magnetic properties of Fe–Mn alloys have long been a subject of great interest and debate, with various works reporting conflicting results of ferromagnetic or antiferromagnetic coupling.^{51–53} Recent findings have concluded that the nature of coupling is very sensitive to various conditions and that the majority coupling-type may switch depending on the concentration.^{54,55} Additionally, changes in local charge densities, as would be introduced by the N atoms in Fe_{16}N_2 , have been shown to strongly influence the stability of ferromagnetic and antiferromagnetic coupling for Mn impurities in bcc and fcc Fe.⁵⁶ Hence, our results support these recent reports while also extending the understanding of magnetic properties to the novel system of $\text{Fe}_{16-x}\text{Mn}_x\text{N}_2$.

The prediction of large, ferromagnetically-coupled Mn magnetic moments in $\text{Fe}_{16-x}\text{Mn}_x\text{N}_2$ is supported by the earlier theoretical works of Huang *et al.*²³ and Ke *et al.*,¹⁸ in which moments as high as $3.1 \mu_B$ and $3.23 \mu_B$ were calculated within the framework of GGA and GW, respectively. In terms of experimental work, data remain limited, generally showing minor decreases in magnetization at relatively high concentrations (5%–15%).^{22,57} To provide further insight, we have performed a detailed investigation into the properties of this system at lower Mn concentrations. Firstly, we have determined which site Mn prefers to occupy at sufficiently low

concentrations, in which individual Mn impurities remain isolated from one another. The formation energies of the $\text{Fe}_{16-x}\text{Mn}_x\text{N}_2$ alloy, with respect to pure Fe_{16}N_2 , for Mn atoms placed at the $4d$, $4e$, and $8h$ sites at a concentration of approximately 1.5% are found to be -16.6 , -6.74 , and -8.72 meV/atom, respectively, indicating that Mn occupation is preferred at the $4d$ site. When placed at this site, Mn couples ferromagnetically and achieves a very high magnetic moment of $3.712 \mu_B$. To determine how this influences the overall magnetic properties of the material, we have calculated the average magnetic moment per metal atom as a function of Mn concentration when placed solely at $4d$ sites, the results of which are listed in Table II. Interestingly, the overall average magnetic moment exhibits a linear increase at low concentrations, reaching a maximum of $2.880 \mu_B$ at approximately 4.68%. However, if Mn impurities occupy the $4d$ sites at concentrations of 6.25% or greater, the magnetic moment begins to deteriorate. This change is directly related to the effects of Mn on neighboring Fe atoms. At sufficiently low concentrations, Mn impurities remain isolated and cause only a slight decrease ($<0.05 \mu_B/\text{Fe}$) in the magnetic moments of surrounding Fe atoms. However, at higher concentrations, Mn atoms placed at the $4d$ sites are forced to share adjacent Fe–N clusters, causing a larger decrease ($\sim 0.15 \mu_B/\text{Fe}$) in the surrounding Fe atoms. Further explanations of the magnetic coupling from an electronic and chemical perspective are given in Sec. III D.

As listed in Table II, placing Mn atoms at $4d$ sites causes small contraction of the unit cell (-0.35% at a Mn concentration of 6.25%) as a result of the smaller atomic radius of Mn. Therefore, by considering changes in volume and average magnetic moment, we have calculated the volume magnetization of $\text{Fe}_{16-x}\text{Mn}_x\text{N}_2$ at low concentrations. Table II shows that magnetization is increased and reaches a maximum of about 2.134 MA/m, corresponding to a 1.41% increase with respect to pure Fe_{16}N_2 . The possibility of a greater increase in magnetization may exist at finer concentrations; however, we are limited by viability based on computational expense. We stress that these results provide insight into only the magnetization of the system, which may or may not lead to higher coercivity. Furthermore, we suggest additional experimental work be conducted to confirm these findings and investigate a more detailed range of concentrations.

Average magnetic moments of the end-member compounds have been calculated, with the resulting values listed in Table I. All systems are shown to exhibit smaller moments than Fe_{16}N_2 . Two compounds, Co_{16}N_2 and Ni_{16}N_2 , are ferromagnetic and achieve relatively high moments of 1.937 and $0.718 \mu_B$, respectively. As is the

TABLE II. Structural, energetic, and magnetic properties of $\text{Fe}_{16-x}\text{Mn}_x\text{N}_2$ at low concentrations, calculated using the hybrid HSE06 functional. Alloy concentrations listed are given by $(x/16) \times 100\%$. Mn substitution is considered only at the energetically favorable $4d$ sites. The magnetic moments listed are averages of all metal atoms (Fe and Mn) in the structure. Volumes listed are normalized per formula unit of Fe_{16}N_2 . Formation energies are with respect to pure Fe_{16}N_2 .

| Mn concentration (%) | Average moment (μ_B) | Volume (\AA^3) | Magnetization (MA/m) | Formation energy (meV/atom) |
|----------------------|----------------------------|---------------------------|----------------------|-----------------------------|
| 0.00 | 2.844 | 200.486 | 2.103 | 0.00 |
| 1.5625 | 2.857 | 200.449 | 2.113 | -16.6 |
| 3.124 | 2.869 | 200.248 | 2.124 | -32.8 |
| 4.6875 | 2.880 | 200.074 | 2.134 | -51.7 |
| 6.25 | 2.849 | 199.889 | 2.113 | -56.6 |

case with Fe_{16}N_2 and Fe, these magnetic moments are higher than those of Co and Ni in their respective ground states. The other end-member compounds in this work are ferrimagnetic due to metal atoms at the $4d$, $4e$, and $8h$ sites exhibiting antiparallel magnetic moments of unequal magnitudes. Mn_{16}N_2 is the only compound of this type to exhibit any significant average magnetic moment ($0.188 \mu_B$), whereas the rest display near-zero values.

D. Electronic structure

The spin-polarized electronic density of states (DOS) for pure Fe_{16}N_2 is shown in Fig. 4(a). General features of the DOS match well with previous calculations.¹⁷ Covalent interaction between Fe $3d$ and N $2p$ electrons is shown by strong hybridization in two

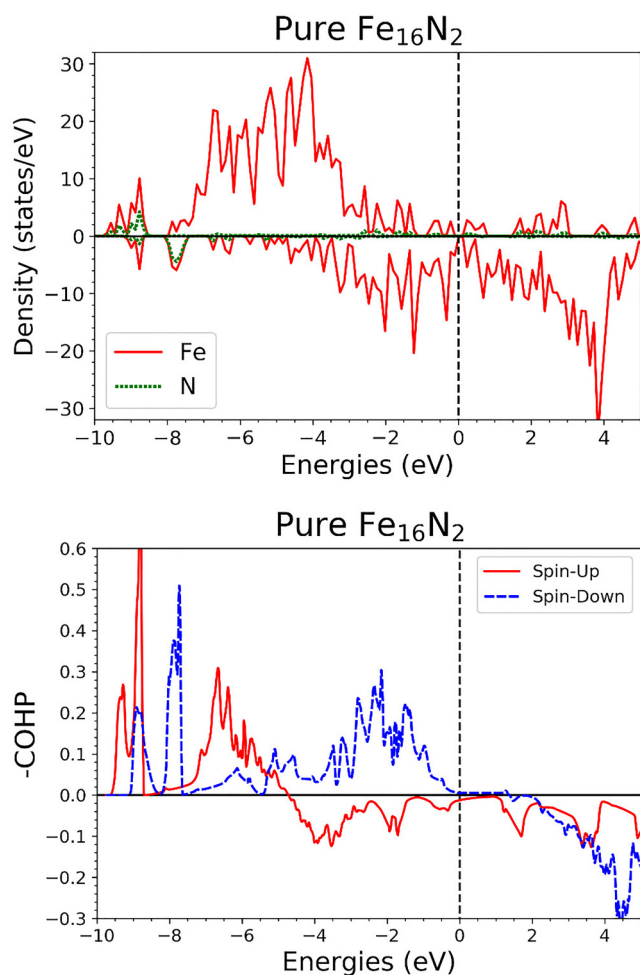


FIG. 4. Spin-polarized (a) electronic density of states (DOS) and (b) COHP curves for pure Fe_{16}N_2 , calculated using the hybrid HSE06 functional. In the DOS, spin-up densities are plotted above the x-axis, while spin-down densities are plotted below. For -COHP, positive values indicate bonding, while negative values indicate antibonding. For both figures, the Fermi energy is set to 0 eV.

regions: -9 eV for spin-up states and -7 eV for spin-down states. Significant Fe–N bonding occurs only for Fe atoms at the $4e$ and $8h$ sites, which neighbor N atoms. The majority of remaining occupied states consist of itinerant Fe d electrons involved in metallic bonding, occurring mostly between Fe atoms at the $4d$ sites and surrounding Fe atoms at $4e$ and $8h$ sites. Hence, these features reflect the roles of both localized and itinerant electrons within Fe_{16}N_2 .¹⁶ The spin-polarized DOS indicates much greater occupation of Fe spin-up states compared to spin-down states, leading to the large net magnetic moment discussed in Sec. III D.

Other work has emphasized the importance of valence electron concentration and covalent interactions on the stability of transition metal nitrides and carbides.^{58–61} Thus, to gain further insight into the nature of bonding in Fe_{16}N_2 , we have computed Crystal Orbital Hamiltonian Populations (COHP), providing another method for analyzing the electronic structure. In COHP analysis, the electronic density of states is decomposed into orbital overlap populations, allowing states to be broken down into categorical covalent interactions.^{62–66} Specifically, bonding and antibonding states correspond to energetically favorable and unfavorable orbital overlap, respectively, arising from the Pauli exclusion principle as discussed in more detail through previous texts.^{67,68} Here, we utilize the LOBSTER package^{62–66} to compute COHP with the convention of inverting sign (-COHP) such that positive and negative values represent bonding and antibonding states, respectively.⁶⁹ Following the approach of Landrum and Dronskowski,⁷⁰ we have considered both the nonmagnetic and ferromagnetic configurations of Fe_{16}N_2 . Such magnetic ordering is included in COHP by partitioning the spin-polarized charge density determined throughout our DOS calculations. As shown in Fig. S3 of the [supplementary material](#), the nonmagnetic COHP curves display strong antibonding character at the Fermi energy, causing a ferromagnetic configuration to become energetically favorable. The COHP curves of ferromagnetic Fe_{16}N_2 are displayed in Fig. 4(b). Indeed, integration of COHP (-IpCOHP) within the range of occupied energies, which provides an estimate of bond strength, yields a value of 0.994 eV for the ferromagnetic configuration. This is larger than the value of 0.838 eV for the nonmagnetic configuration, indicating enhanced covalent interaction and a more stable configuration. At low energies ranging from -10 to -7 eV, the ferromagnetic COHP exhibits strong bonding character as a result of Fe–N covalent bonding. At moderate energies, ranging from -7 to -4.5 eV, interactions between spin-up and -down states are purely bonding due to d orbital overlap between adjacent Fe atoms. However, at energies above -4.5 eV, spin-up states display relatively significant antibonding character while spin-down states remain purely bonding. Considering that a majority of the Fe $3d$ electrons are spin-up, occupation of antibonding states is a direct result of the Pauli exclusion principle. The occupation of these antibonding states is likely a key factor in the low thermal stability of Fe_{16}N_2 .

To provide further explanation for the influence of each transition metal on the energetic and magnetic properties of Fe_{16}N_2 , electronic DOS has been calculated for each $\text{Fe}_{16-x}\text{M}_x\text{N}_2$ alloy. Corresponding results are displayed in Fig. S4 of the [supplementary material](#). As discussed in Sec. III C, group (i) elements Mn, Co, and Ni couple ferromagnetically with Fe while group (ii) elements Ti, V, and Cr couple antiferromagnetically. This finding is reflected

by the local DOS of the respective transition metal in each alloy. Group (i) elements are characterized by a majority occupation of spin-up states while group (ii) elements display a majority occupation of spin-down states. The nature of coupling for each transition metal can be explained using the Stoner model, which states that intra-atomic exchange (Hund's rules) and electronic occupation at the Fermi energy must both be sufficiently strong to cause ferromagnetic ordering.⁷¹ Excluding Mn, elements lying to the left of Fe on the periodic table (Ti, V, Cr) contribute insufficient 3d electrons and display relatively weak intra-atomic exchange; hence, antiferromagnetic coupling is favorable. In contrast, elements lying to the right of Fe (Ni, Co) contribute more electrons and display stronger intra-atomic exchange; hence, ferromagnetic coupling is favorable. The findings here match with the magnetic ordering of each transition metal in its respective elemental ground state. Mn represents a unique case for which separate analysis is conducted later in this section.

To determine the cause of stabilization in $\text{Fe}_{16-x}\text{Mn}_x\text{N}_2$ alloys from a chemical and electronic perspective, COHP has been calculated for each system. As with all other properties discussed thus far, clear distinction in features of the COHP is observed between alloys of group (i) and group (ii) transition metals. The group (i) alloys of Ti, V, and Cr display greater overall bonding character than group (ii) alloys of Mn, Ni, and Co. As discussed earlier and shown in Fig. 4(b), the spin-up electrons of Fe occupy antibonding orbitals at energies above -4.5 eV while the spin-down states maintain purely bonding character throughout all occupied energies. Hence, the group (i) elements, which couple antiferromagnetically, exhibit decreased occupation of the spin-up antibonding states and increased occupation of the spin-down bonding states. This enhanced covalent interaction results in a greatly decreased formation energy, as shown in Fig. 3. In contrast, the group (ii) elements, which couple ferromagnetically, retain majority occupation of the spin-up antibonding states. However, compared to the electronic configuration of the Fe atoms in pure Fe_{16}N_2 , the group (ii) elements exhibit slightly greater occupation of spin-down orbitals with bonding character. As a result, a decrease in formation energy is observed, though to a lesser degree than in the group (i) alloys. These conclusions are supported by $-\text{IpCOHP}$ values, found by integrating the COHP curves, listed in Table S4 of the [supplementary material](#). Alloying causes an increase in $-\text{IpCOHP}$ for all metals in this work, thus strengthening covalent interactions and stabilizing the material. Distinction is shown between group (i) and group (ii) elements, with the former exhibiting greater values of $-\text{IpCOHP}$ than the latter. Within each group, trends in formation energies are related to electronegativities. Transition metals displaying lower electronegativities, therefore forming more highly ionic metal-nitrogen bonds, are found to cause a greater decrease in formation energy. These findings are supported by charge transfer values of each element, listed in Table S5 of the [supplementary material](#).

As discussed in Sec. III C, Mn is the only transition metal in this work to cause an increase in magnetization when alloyed with Fe_{16}N_2 at low concentrations ($<5\%$). Considering our results here, in addition to previous findings regarding the interaction of Mn in bcc Fe and in Fe_{16}N_2 ,^{23,53,57} we hypothesize that the interstitial N atoms are crucial in stabilizing the ferromagnetic coupling and

high magnetic moment of Mn in $\text{Fe}_{16-x}\text{Mn}_x\text{N}_2$. To test this theory, we have computed several key electronic properties in $\text{Fe}_{16-x}\text{Mn}_x\text{N}_2$, with a single isolated Mn impurity at the 4d site, for two cases: with and without interstitial N atoms included in a 72-atom supercell. The structure is kept fixed for each case, allowing solely electronic effects of the N atoms to be analyzed. This procedure follows the work of Sims *et al.*, in which the fictitious " Fe_{16}N_0 " structure was studied to determine the influence interstitial N atoms on the electronic structure of Fe atoms.¹⁷ They concluded that magnetic moments in Fe_{16}N_0 are larger than those of bcc Fe owing to volumetric expansion, whereas the addition of N atoms further increases surrounding Fe moments as strong exchange splitting is induced.¹⁷ In this work, we find similar results which are enhanced in the electronic structure of Mn. Firstly, the effective charge of Mn is calculated using Bader's analysis. Without nitrogen atoms in the structure, Mn exhibits an effective valence charge of $6.847e$, indicating a net transfer of only $0.153e$ to surrounding Fe atoms. In contrast, including N atoms causes the charge transfer to substantially increase, resulting in a value of $0.288e$. Therefore, although Mn atoms at the 4d sites are not directly coordinated to N atoms, an indirect electrostatic interaction is mediated by adjacent Fe atoms. Next, to determine how this change in charge density affects spin-up and -down states individually, we have calculated the spin-polarized local electronic DOS of Mn in each case. As displayed in Fig. 5, inclusion of N atoms causes two major changes in the DOS. Firstly, occupation of spin-up states is greatly enhanced, reflected by a shift in the density peak from above to below the Fermi energy. Secondly, occupation of spin-down states is decreased. Each of these effects results in a ferromagnetic configuration with a large net moment.

To provide a fundamental explanation for this phenomenon, we consider the competition between intra- and interatomic exchange interactions. Intra-atomic exchange occurs within the Mn atom and is linked to Hund's rules, stating the lowest energy atomic configuration is that which maximizes the total spin within a subshell.⁷¹ Interatomic exchange occurs between Mn and surrounding Fe atoms due to the Pauli exclusion between electrons of like spin. Our analysis of effective charge demonstrated that both Fe and Mn retain a greater majority of their individual electrons without the inclusion of N atoms. As a result, a strong overlap of occupied 3d orbitals occurs, causing the interatomic exchange interaction to dominate; hence, as shown by the local DOS without N atoms included, a forced occupation of spin-down states takes place, coupled with a decrease in the occupation of spin-up states. Whereas for the other case, introducing N atoms allows significantly increased charge transfer away from the Fe and Mn atoms, thus decreasing the overlap of occupied 3d orbitals and allowing intra-atomic exchange to dominate. According to Hund's rules, a majority occupation of spin-up states is preferred in this configuration, as shown by the local DOS with N atoms included. Therefore, by means of increased intra-atomic exchange and decreased interatomic interaction, the net result of the interstitial N atoms is the stabilization of ferromagnetic Mn coupling with an enhanced magnetic moment. We note that the mechanism described here is similar to that of the known Mn-based Heusler alloys, which also achieve exceptionally high localized magnetic moments at Mn sites owing to numerous effects

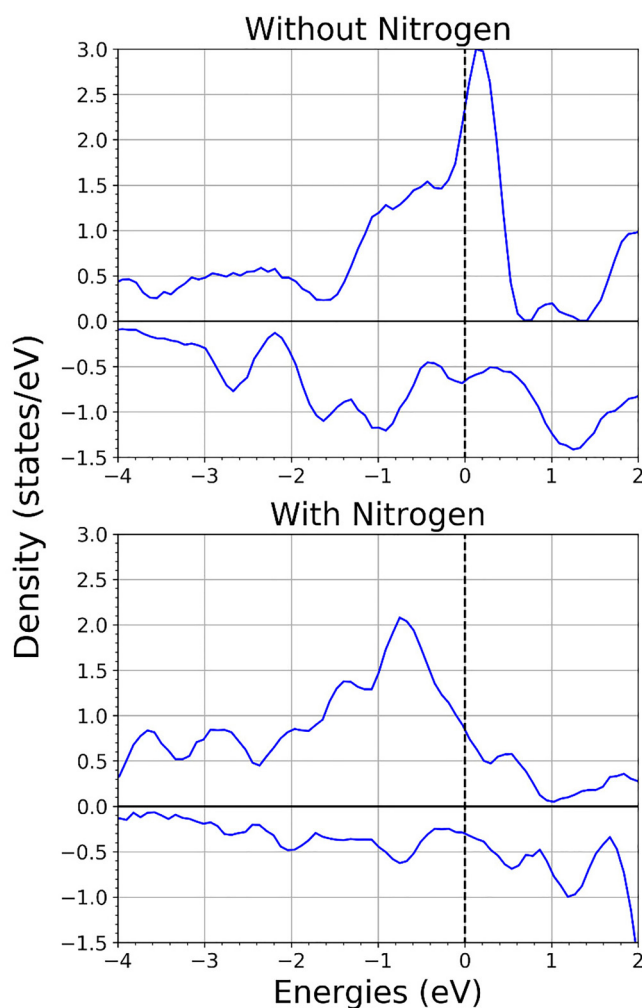


FIG. 5. Local electronic density of states (DOS), calculated using GGA, for isolated Mn atoms placed at the $4d$ sites within a 72-atom supercell, $\text{Fe}_{63}\text{Mn}_1\text{N}_{16}$, (a) without and (b) with interstitial nitrogen atoms included. Spin-up densities are plotted above the x -axis, while spin-down densities are plotted below. The Fermi energy is set to 0 eV.

including volumetric expansion and increased charge localization with respect to the end-member compounds.^{72–74}

Stabilization of ferromagnetic Fe–Mn coupling may also be viewed from a chemical perspective. We have calculated COHP with respect to Mn and its surrounding Fe atoms, within structures including and excluding the interstitial N atoms. In a similar manner to the analysis conducted on pure Fe_{16}N_2 earlier in this section, we first calculate COHP curves for nonmagnetic configurations, the results of which are displayed in Fig. S5 of the [supplementary material](#). If no N atoms are included, the Fermi level is shown to fall directly within a region of nonbonding. In contrast, the inclusion of N atoms causes the Fermi level to shift into a region of strong antibonding. Therefore, it becomes energetically

favorable for the electrons to rearrange into a ferromagnetic configuration. This conclusion is supported by the spin-polarized Fe–Mn COHP curves in $\text{Fe}_{16-x}\text{Mn}_x\text{N}_2$, displayed in Fig. S6 of the [supplementary material](#). By adopting a ferromagnetic configuration, the total $-I_p\text{COHP}$ increases from 0.574 eV to 0.628 eV, indicating enhanced covalent interaction with lower energy than the nonmagnetic state.

The electronic DOS has been calculated and plotted for each end-member compound, displayed in Fig. S7 of the [supplementary material](#). As in Fe_{16}N_2 , strong hybridization between the $3d$ electrons of the transition metal and the $2p$ electrons of N occurs at low energies, while the majority of remaining states are occupied by itinerant $3d$ electrons. However, features of the metal spin-up and -down states vary depending on the system. The ferromagnetic compounds, Co_{16}N_2 and Ni_{16}N_2 , display a significant majority occupation of spin-up states. However, in contrast to Fe_{16}N_2 , a greater number of spin-down states are occupied as a result of increased d electron contribution from Co and Ni, therefore causing the net magnetic moments of Co_{16}N_2 and Ni_{16}N_2 to be smaller than that of Fe_{16}N_2 . As for the remaining end-member systems, which are only ferrimagnetic, differences between occupations of spin-up and -down states are relatively minor. This result reflects the dominance of interatomic exchange interactions between neighboring atoms of Ti, V, Cr, and Mn. Lastly, regarding the instability of Ti_{16}N_2 discussed in Sec. III A, we perform COHP calculations revealing a low $-I_p\text{COHP}$ value of 0.414 eV for Ti_{16}N_2 in contrast to a much larger value of 0.994 eV for Fe_{16}N_2 , thus confirming our prediction of weak metallic bonds present in Ti_{16}N_2 owing to low valence electron concentration. The detailed COHP curves are displayed in Fig. S8 of the [supplementary material](#).

IV. CONCLUSION

In summary, we have studied the structural, energetic, electronic, and magnetic properties of pure Fe_{16}N_2 and $\text{Fe}_{16-x}\text{Mn}_x\text{N}_2$ alloys using a variety of state-of-the-art computational techniques. Standard DFT approaches based on GGA are shown to provide a reliable description of the structural and energetic properties of Fe_{16}N_2 . However, these methods may be insufficient to accurately predict the electronic structure and magnetization due to the presence of partial electron localization and charge distribution variations resulting from interstitial N atoms.^{12,17} Therefore, the hybrid HSE06 functional is utilized to calculate a magnetic moment of $2.844 \mu_B/\text{Fe}$ and a volume magnetization of 2.103 MA/m in Fe_{16}N_2 . If confirmed, these results would support the high magnetization suggested by recent experimental work;¹⁰ however, the accuracy of hybrid functionals must be considered carefully as the most suitable choice of screening and mixing parameters may vary depending on the strength of exchange-correlation effects occurring within the metallic system.¹⁷

In $\text{Fe}_{16-x}\text{Mn}_x\text{N}_2$ alloys, simulated using special quasirandom structures, we have illustrated direct relationships between changes in volume and atomic radii of the transition metals, while changes in the c/a ratio are more closely related to magnetic effects. Formation energies of all alloys are shown to decrease as alloy concentration is increased, indicating enhanced stabilization. We predict $\text{Fe}_{13}\text{Ti}_3\text{N}_2$ and $\text{Fe}_{13}\text{V}_3\text{N}_2$ to remain stable up to temperatures

of 930 K and 775 K, respectively, both of which are significantly higher than the known decomposition temperature of pure Fe_{16}N_2 . However, large decreases in magnetization limit the suitability of these materials for applications. Should Ti and V be used as alloying elements in Fe_{16}N_2 , low concentrations are recommended. Trends in formation energies are linked to differences in covalent interactions and electronegativities, shown by COHP curves and effective charges. For almost all transition metals tested, increasing concentration in $\text{Fe}_{16-x}\text{M}_x\text{N}_2$ leads to a decrease in magnetization. The degree of impact can be explained in terms of magnetic coupling. Group (i) elements Ti, V, and Cr couple antiferromagnetically with surrounding Fe atoms and cause a large decrease in net magnetization. In contrast, group (ii) elements Ni and Co couple ferromagnetically and cause only a small decrease in net magnetization.

$\text{Fe}_{16-x}\text{Mn}_x\text{N}_2$ alloys represent a unique case. At low concentrations (<5%), we have predicted a 1.41% enhancement in magnetization using the HSE06 functional. This results from ferromagnetic coupling and large local magnetic moment ($3.71\mu_B$) of Mn atoms within the structure. By analyzing the electronic, chemical, and magnetic properties of the $\text{Fe}_{16-x}\text{Mn}_x\text{N}_2$ with and without the inclusion of interstitial N atoms, we provided clear evidence that the N atoms are crucial in stabilizing the ferromagnetic configuration of Mn atoms. This is done by changing the relative magnitudes of intra- and interatomic exchange interactions. At intermediate concentrations (5%–20%), magnetization of the system remains relatively constant as large Mn moments are offset by decreases in Fe moments. At concentrations greater than 20%, magnetization decreases significantly as a portion of the Mn population begins to couple antiferromagnetically. We note that these findings must be considered cautiously, as the hybrid HSE06 functional risks the overestimation of exchange-splitting in metallic systems. Furthermore, only magnetization has been studied in this work, while further investigation is necessary to determine the changes in coercivity in $\text{Fe}_{16-x}\text{Mn}_x\text{N}_2$ at low concentrations.

Lastly, the properties of the end-member M_{16}N_2 compounds have been computed. Given that none of these materials, excluding Fe_{16}N_2 , have been synthesized, we provide purely predictive findings. Except for Ti_{16}N_2 , all are shown to be dynamically stable at 0 K. The instability of Ti_{16}N_2 can be attributed to its low valence electron concentration. Formation energies of the end-member compounds indicate that trends in energies of the $\text{Fe}_{16-x}\text{M}_x\text{N}_2$ alloys follow a mostly linear path as concentration is increased. With respect to magnetic properties, Co_{16}N_2 and Ni_{16}N_2 are the only materials exhibiting ferromagnetic configurations. The rest are ferrimagnetic with near-zero net magnetizations.

SUPPLEMENTARY MATERIAL

See the [supplementary material](#) for further information regarding the detailed structural, thermodynamic, and electronic properties of $\text{Fe}_{16-x}\text{M}_x\text{N}_2$ alloys and M_{16}N_2 end-members where M represents 3d transition metals Ti, V, Cr, Mn, Co, and Ni. An additional 8 figures and 5 tables include equilibrium lattice parameters, formation energies, magnetizations, $-I_p\text{COHP}$ values, effective charges, phonon DOS, electronic DOS, and COHP curves. SQS files organized by composition are also made available for each compound.

ACKNOWLEDGMENTS

The computing for this project was performed at the Ohio Supercomputer Center (OSC)⁷⁵ and Tandy Supercomputing Center (TSC). The authors thank the CMMI of National Science Foundation (NSF) under Grant Nos. 1629239 and 1629230 for funding this work. The authors also acknowledge support from the Air Force Research Laboratory, Space Vehicles Directorate, under Contract No. FA9453-11-C-0253.

REFERENCES

- ¹S. Sugimoto, *J. Phys. D Appl. Phys.* **44**, 064001 (2011).
- ²O. Gutfleisch, M. A. Willard, E. Brück, C. H. Chen, S. G. Sankar, and J. P. Liu, *Adv. Mater.* **23**, 821 (2011).
- ³M. A. Willard, in *Frontiers on Engineering: Reports on Leading-Edge Engineering from the 2012 Symposium* (National Academies Press, Washington, DC, 2013), p. 57.
- ⁴K. H. Jack, *Proc. R. Soc. A* **208**, 200 (1951).
- ⁵T. K. Kim and M. Takahashi, *Appl. Phys. Lett.* **20**, 492 (1972).
- ⁶Y. Sugita, K. Mitsuoka, M. Komuro, H. Hoshiya, Y. Kozono, and M. Hanazono, *J. Appl. Phys.* **70**, 5977 (1991).
- ⁷J. M. D. Coey *et al.*, *J. Phys. Condens. Matter* **6**, L23 (1994).
- ⁸M. Takahashi *et al.*, *IEEE Trans. Magn.* **29**, 3040 (1993).
- ⁹M. Takahashi, H. Takahashi, H. Nashi, H. Shoji, and T. Wakiyama, *J. Appl. Phys.* **79**, 5564 (1996).
- ¹⁰N. Ji, V. Lauter, X. Zhang, H. Ambaye, and J.-P. Wang, *Appl. Phys. Lett.* **102**, 072411 (2013).
- ¹¹S. Ishida, K. Kitawatase, S. Fujii, and S. Asano, *J. Phys. Condens. Matter* **4**, 765 (1992).
- ¹²A. Sakuma, *J. Appl. Phys.* **79**, 5570 (1996).
- ¹³K. Umino, H. Nakajima, and K. Shiiki, *J. Magn. Mater.* **153**, 323 (1996).
- ¹⁴H. Nakajima, Y. Ohashi, and K. Shiiki, *J. Magn. Mater.* **167**, 259 (1997).
- ¹⁵R. Coehoorn, G. H. O. Daalderop, and H. J. F. Jansen, *Phys. Rev. B* **48**, 3830 (1993).
- ¹⁶N. Ji, X. Liu, and J.-P. Wang, *New J. Phys.* **12**, 063032 (2010).
- ¹⁷H. Sims *et al.*, *Phys. Rev. B* **86**, 174422 (2012).
- ¹⁸L. Ke *et al.*, *Phys. Rev. B* **88**, 024404 (2013).
- ¹⁹E. H. D. M. Van. Voothuysen, D. O. Boerma, and N. C. Chechenin, *Mater. Trans. A* **33**, 2593 (2002).
- ²⁰S. Hirotsawa, M. Nishino, and S. Miyashita, *Adv. Nat. Sci.-Nanosci.* **8**, 013002 (2017).
- ²¹H. Y. Wang and E. Y. Jiang, *J. Phys. Condens. Matter* **9**, 2739 (1997).
- ²²Y. Jiang, B. Himmetoglu, M. Cococcioni, and J.-P. Wang, *AIP Adv.* **6**, 056007 (2016).
- ²³J. Huang, W. Xie, and X. Li, *J. Magn. Magn. Mater.* **364**, 1 (2014).
- ²⁴X. Zhao, C.-Z. Wang, Y. Yao, and K.-M. Ho, *Phys. Rev. B* **94**, 224424 (2016).
- ²⁵D. Benea, O. Isnard, and V. Pop, *J. Magn. Magn. Mater.* **420**, 75 (2016).
- ²⁶S. Matar, *Z. Phys. B* **87**, 91 (1992).
- ²⁷G. Kresse and J. Hafner, *Phys. Rev. B* **47**, 558 (1993).
- ²⁸G. Kresse and J. Hafner, *Phys. Rev. B* **49**, 14251 (1994).
- ²⁹G. Kresse and J. Furthmüller, *Comput. Mater. Sci.* **6**, 15 (1996).
- ³⁰G. Kresse and J. Furthmüller, *Phys. Rev. B* **54**, 11169 (1996).
- ³¹G. Kresse and D. Joubert, *Phys. Rev. B* **59**, 1758 (1999).
- ³²P. E. Blöchl, *Phys. Rev. B* **50**, 17953 (1994).
- ³³N. W. Ashcroft and N. D. Mermin, *Solid State Physics* (Cengage Learning, 1976), Chaps. 24–26, pp. 469–532.
- ³⁴C. M. Varma and W. Weber, *Phys. Rev. Lett.* **39**, 1094 (1977).
- ³⁵E. S. Toberer, A. Zevalkink, and G. J. Snyder, *J. Mater. Chem.* **21**, 15843 (2011).
- ³⁶A. Togo and I. Tanaka, *Scr. Mater.* **108**, 1 (2015).

- ³⁷A. Zunger, S.-H. Wei, L. G. Ferreira, and J. E. Bernard, *Phys. Rev. Lett.* **65**, 353 (1990).
- ³⁸A. van de Walle and G. Ceder, *J. Phase Equilib.* **23**, 348 (2002).
- ³⁹A. van de Walle and M. Asta, *Model. Simul. Mater. Sci. Eng.* **10**, 521 (2002).
- ⁴⁰A. van de Walle, M. Asta, and G. Ceder, *Calphad* **26**, 539 (2002).
- ⁴¹A. van de Walle, *Calphad* **33**, 266 (2009).
- ⁴²G. L. W. Hart and R. W. Forcade, *Phys. Rev. B* **77**, 224115 (2008).
- ⁴³A. van de Walle *et al.*, *Calphad* **42**, 13 (2013).
- ⁴⁴Y.-R. Jang and B.-D. Yu, *J. Magn.* **16**, 201 (2011).
- ⁴⁵J. Paier *et al.*, *J. Chem. Phys.* **124**, 154709 (2006).
- ⁴⁶J. Paier, M. Marsman, and G. Kresse, *J. Chem. Phys.* **127**, 024103 (2007).
- ⁴⁷J. Heyd, G. E. Scuseria, and M. Ernzerhof, *J. Chem. Phys.* **124**, 219906 (2006).
- ⁴⁸D. C. Sun, E. Y. Jiang, and D. Sun, *Thin Solid Films* **298**, 116 (1997).
- ⁴⁹L. Brewer, *Science* **161**(3837), 115 (1968).
- ⁵⁰Y. J. Shi, Y. L. Du, and G. Chen, *Physica B* **407**, 3423 (2012).
- ⁵¹G. Rahman, I. G. Kim, H. K. D. H. Bhadeshia, and A. J. Freeman, *Phys. Rev. B* **81**, 184423 (2010).
- ⁵²N. I. Medvedeva, D. Van Aken, and J. E. Medvedeva, *J. Phys. Condens. Matter* **22**, 316002 (2010).
- ⁵³P. Radhakrishna and F. Livet, *Solid State Commun.* **25**, 597 (1978).
- ⁵⁴N. I. Kulikov and C. Demangeat, *Phys. Rev. B* **55**, 3533 (1997).
- ⁵⁵A. A. Mirzoev, M. M. Yalalov, and D. A. Mirzaev, *Phys. Met. Metallogr.* **101**, 341 (2006).
- ⁵⁶A. Schneider, C.-C. Fu, and C. Barreteau, *Phys. Rev. B* **98**, 094426 (2018).
- ⁵⁷X. Bao, R. M. Metzger, and M. Carbucicchio, *J. Appl. Phys.* **75**, 5870 (1994).
- ⁵⁸X. Zhou, D. Gall, and S. V. Khare, *J. Alloys Compd.* **595**, 80 (2014).
- ⁵⁹J. A. Warner, S. K. R. Patil, S. V. Khare, and K. C. Masiulaniec, *Appl. Phys. Lett.* **88**, 101911 (2006).
- ⁶⁰K. Balasubramanian, S. Khare, and D. Gall, *Phys. Rev. B* **94**, 174111 (2016).
- ⁶¹S.-H. Jhi, J. Ihm, S. G. Louie, and M. L. Cohen, *Nature* **399**, 132 (1999).
- ⁶²R. Dronskowski and P. E. Blöchl, *J. Phys. Chem.* **97**, 8617 (1993).
- ⁶³V. L. Deringer, A. L. Tchougreeff, and R. Dronskowski, *J. Phys. Chem. A* **115**, 5461 (2011).
- ⁶⁴S. Maintz, V. L. Deringer, A. L. Tchougreeff, and R. Dronskowski, *J. Comput. Chem.* **34**, 2557 (2013).
- ⁶⁵S. Maintz, V. L. Deringer, A. L. Tchougréeff, and R. Dronskowski, *J. Comput. Chem.* **37**, 1030 (2016).
- ⁶⁶S. Maintz, M. Esser, and R. Dronskowski, *Acta Phys. Pol. B* **47**, 1165 (2016).
- ⁶⁷W. A. Harrison, *Electronic Structure and the Properties of Solids: The Physics of the Chemical Bond (Dover Books on Physics)* (Dover Publications, 1989).
- ⁶⁸R. Hoffman, *Solids and Surfaces: A Chemist's View of Bonding in Extended Structures* (Wiley, 1989).
- ⁶⁹S. Steinberg and R. Dronskowski, *Crystals* **8**, 225 (2018).
- ⁷⁰G. A. Landrum and R. Dronskowski, *Angew. Chem. Int. Ed. Engl.* **39**, 1560 (2000).
- ⁷¹S. Blundell, *Magnetism in Condensed Matter* (Oxford University Press, 2001).
- ⁷²J. Kübler, A. R. Williams, and C. B. Sonners, *Phys. Rev. B* **28**, 1745 (1983).
- ⁷³C. C. M. Campbell, *J. Magn. Magn. Mater.* **3**, 354 (1976).
- ⁷⁴J. Karel *et al.*, *Phys. Chem. Chem. Phys.* **17**, 31707 (2015).
- ⁷⁵See <http://osc.edu/ark:/19495/f5s1ph73> for Ohio-Supercomputer-Center (1987).
- ⁷⁶K. Momma and F. Izumi, *J. Appl. Crystallogr.* **44**, 1272 (2011).